coatings

MDPI

Article

Chemical Vapor Deposition of Bi-Te-Ni-Fe on Magnesium Oxide Substrate and Its Seebeck Effect

Yong X. Gan [1,*], Anan S. Hamdan [2], Jeremy B. Gan [3] and Mingheng Li [4]

1 Department of Mechanical Engineering, College of Engineering, California State Polytechnic University, Pomona, 3801 W Temple Avenue, Pomona, CA 91768, USA
2 Department of Electromechanical Engineering Technology, California State Polytechnic University, Pomona, 3801 W Temple Avenue, Pomona, CA 91768, USA; ashamdan@cpp.edu
3 Diamond Bar High School, 21400 Pathfinder Road, Diamond Bar, CA 91765, USA; jeremygan49@yahoo.com
4 Department of Chemical and Materials Engineering, California State Polytechnic University, Pomona, 3801 W Temple Avenue, Pomona, CA 91768, USA; minghengli@cpp.edu
* Correspondence: yxgan@cpp.edu; Tel.: +1-909-869-2388; Fax: +1-909-869-4341

Received: 16 August 2017; Accepted: 29 September 2017; Published: 1 October 2017

Abstract: In this work, a Bi-Te-Ni-Fe complex coating material was obtained on magnesium oxide substrate by a single step ambient pressure chemical vapor deposition (CVD). Nickel acetate, bismuth acetate, iron (III) nitrate, and tellurium (IV) chloride dissolved in *N*,*N*-dimethylformamide (DMF) served as the metal sources for Ni, Bi, Fe, and Te, respectively. Hydrogen was used as the carrier gas. The substrate was kept at 500 °C in a quartz tube reaction chamber. The chemical vapor deposition time was two hours. Scanning electron microscopic observation revealed porous morphology of the deposited material with a needle-like submicron fine structure. These needle-like entities form networks with fairly uniform distribution on the substrate. Thermoelectric property test showed that the coating is p-type with a Seebeck coefficient of 179 μV/K. Time-dependent potential data were obtained to show the sensitivity of the Seebeck effect to temperature changes.

Keywords: ambient pressure chemical vapor deposition; coating; dendritic structure; Seebeck effect

1. Introduction

Chemical vapor deposition (CVD) is a bottom-up approach to make micro or nanoscale materials. It has found applications in processing low dimension thermoelectric materials. There are many types of CVDs including ambient pressure CVD, photo-thermal CVD, metal-organic CVD, plasma enhanced CVD, ion beam CVD, etc. As the simplest form, the ambient pressure deposition has been used to make Bi_2Se_3 nanowires on graphite papers without using catalysts [1]. The rate of deposition in CVD is typically higher than that in physical vapor deposition (PVD). For example, a high deposition rate was achieved to deposit SrB_6 coating on a sapphire substrate [2]. The obtained SrB_6 coating is n-type. Another feature of CVD is that the structure of a deposited material changes with pre-patterned metal dot catalysts [3] and the CVD conditions. This is shown by depositing nitrogen doped diamond coatings on a graphite substrate followed by a peeling-off step to obtain free-standing films [4]. Methane, nitrogen, and hydrogen were inducted into a microwave plasma chemical vapor deposition reactor. A change in different gas flow rates resulted in a change of morphology of the sample from a dense structure without nitrogen to a needle-like porous structure with high flow rate of nitrogen. The nitrogen doped carbon film shows n-type behavior.

CVD has been used for depositing various thermoelectric materials. CVD carbon based thermoelectric materials such as carbon nanotubes and wires [5–7], diamond and diamond-like carbon films [8–13] have been extensively studied. Another family of thermoelectric materials made by CVD includes silicon and silicon compound materials, including silicon nanowires [14,15],

SiC [16,17], and silicon-based compounds [18–21]. Still another category is the pure boron or boron related compounds [22–30]. CVD was reported for preparing oxide thermoelectric materials [31], Ge nanocones [32], and some less common compounds such as Se-C films [33]. Metal-organic chemical vapor deposition (MOCVD) has caught attention and been used for depositing Bi-Te and Sb-Te thermoelectric films [34–36]. Typically, simple metal alkyl complexes are used as precursors. The pyrolysis of these precursors requires a relatively high temperature leading to the incorporation of impurities such as carbon into the deposited film. In the work performed by Bendt et al. [37], a thermolabile precursor, $(Et_2Sb)_2Te$, was used. The $(Et_2Sb)_2Te$ compound is a stable liquid at room temperature with relatively high volatility. The temperature for depositing Sb_2Te_3 films in the MOCVD process was as low as 200 °C using such a precursor.

Recently, processing Bi-Te coatings via MOCVD has caught much attention. Kang et al. [38] used a combination of optimized bismuth and tellurium precursors to deposit bismuth telluride thin films on glass. Triethyl bismuth and di-tertiarybutyl tellurium were the precursors. At low temperature of 300 °C with hydrogen as the protective gas, good quality films were obtained. Single crystal Bi-Te nanowires can be grown from Bi- and Te-bearing metalorganic precursors [39]. The high quality nanostructured wires were studied as topological insulators. By using a single precursor during the low pressure chemical vapor deposition process, Benjamin et al. [40] found that the orientation of nanostructured Bi_2Te_3 topological insulators could be well controlled, leading to the improved thermoelectric efficiency of Bi_2Te_3. In view of the precursor design, careful balancing between volatility, thermal stability, and reactivity needs to be achieved [41]. It has been reported that high quality Bi_2Te_3 topological insulator films grown on GaAs (001) substrates showed high resistivity and high electron mobility, leading to a relatively low Seebeck coefficient [42]. While in the work performed by You et al. [43], fabricating Bi_2Te_3 films by a modified MOCVD system was carried out. Enhanced thermoelectric performance was found with the control of grain size.

In order to precisely control the crystallographic plane of the Bi-Te film, Sun et al. [44] prepared Bi_2Te_3 films with (001) orientation by chemical vapor deposition on pre-synthesized Bi films. The (001) orientation of the Bi_2Te_3 enhanced the transport of the carrier in the films. Kwon et al. [45,46] made bismuth telluride-based alloy thin film for building thermoelectric devices. Complex structures of different conduction types of thermoelectric elements were made [45]. Films on surface-treated sapphire substrates showed better quality. The surface treatment included soaking the sapphire substrates in a potassium-containing solution. The potassium-containing solution facilitated the nucleation of Bi-Te films. The grains of the films were epitaxially oriented. But the films grown on the untreated substrates had multi-orientations, resulting in a random-sized and island-like morphology [46].

The objective of this work was to prepare a Bi-Te-Ni-Fe material on oxide substrate by metal organic chemical vapor deposition (MOCVD). Nickel acetate, bismuth acetate, iron (III) nitrate, and tellurium (IV) chloride dissolved in *N*,*N*-dimethylformamide (DMF) were used as the precursors for Ni, Bi, Fe and Te, respectively. Hydrogen was used as the carrier gas. The structure of the deposited coating was analyzed by scanning electron microscopy. The Seebeck coefficient of the coating was measured to determine the thermoelectric response of the coating. Time-dependent potential measurement was also done to demonstrate the sensitivity of the coating to temperature changes.

2. Materials and Experimental Methods

The chemicals, nickel acetate, bismuth acetate, iron (III) nitrate, tellurium (IV) chloride, and *N*,*N*-dimethylformamide (DMF), were purchased from Alfa Aesar (Ward Hill, MA, USA). The precursor solution was made by dissolving nickel acetate, bismuth acetate, iron (III) nitrate, tellurium (IV) chloride into *N*,*N*-dimethylformamide (DMF) in a 250 mL bottle. The nominal concentration for nickel acetate was 1.0 M and for iron (III) nitrate 0.5 M. The concentration of bismuth acetate was 0.1 M and for tellurium (IV) chloride, the concentration was 0.05 M. The boiling point of DMF is 196 °C. The solution was kept at 90 °C to facilitate vaporizing of the solvent. Hydrogen gas was inducted

into the solution to carry the volatiles into a quartz reaction chamber (marked as part 4 in Figure 1) containing a MgO ceramic plate (marked as part 7 in Figure 1) as the substrate for film deposition because MgO is fairly stable in hydrogen. Glass was not suitable to be used as the substrate because SiO_2 tends to form volatile gas SiH_4. The size of the plate is 153 mm in length, 2 mm in thickness and 38 mm in width. Figure 1 shows the configuration of the reactor. Before reaction, the quartz tube was vacuumed to a low pressure of 10^{-2} Torr. Then, the hydrogen check valve was opened carefully to sustain a volume flow rate of 5 standard cubic centimeters per minute (sccm). After that, the furnace was heated up at a rate of 5 °C/min. The temperature of the reactor was kept at 500 °C using an MTI GSL-1100X-S50 split furnace (MTI Corp, Richmond, CA, USA) (marked as part 5 in Figure 1). The selected temperature of 500 °C was a trade-off between the reaction rate and prevention of Bi evaporation. The total pressure was 1 atm. The precursor was saturated in the hydrogen carrier gas. These conditions were chosen to minimize the cost for fabricating the coating. During the reaction, the exhausting gas was inducted into a container (marked as part 9 in Figure 1) filled with icy water, which allows the vapor to condense. The by-products from CVD reactions such as hydrogen chloride and nitrogen oxide were further trapped in another container (marked as part 10 in Figure 1) and neutralized by sodium carbonate solution. Finally, the remaining hydrogen gas was burned using a stainless steel torch (marked as part 11 in Figure 1). After reaction for 2 h, the deposited specimen was cooled down naturally with the furnace. The thickness of the coating reached about 200 μm.

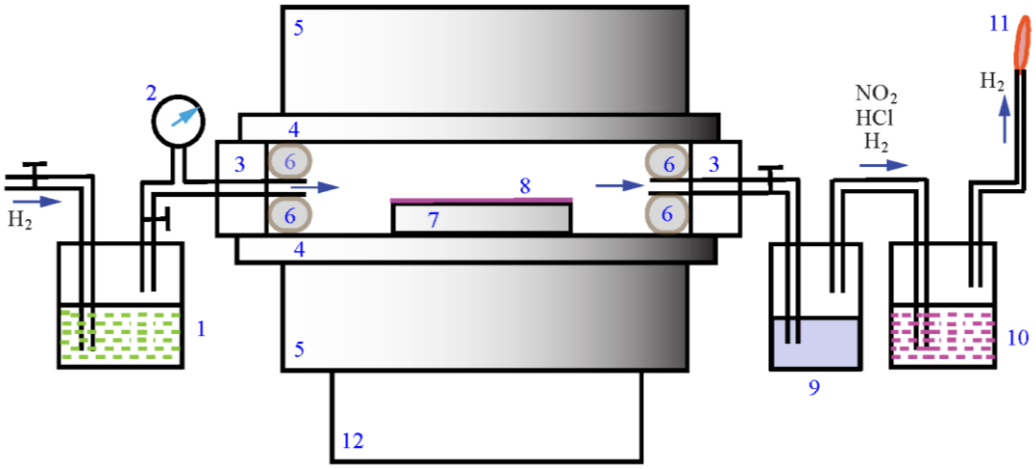

Figure 1. Schematic showing the chemical vapor deposition set-up: 1—precusor solution, 2—vacuum pump with pressure gage, 3—stainless steel vacuum sealing flanges, 4—quartz tube, 5—split furnace, 6—porous alumina thermal insulation blacks, 7—MgO substrate, 8—BiTeNiFe coating, 9—ice container for trapping DMF, 10—sodium carbonate solution, 11—hydrogen burning torch, 12—programmable temperature control unit assembled in the base of the furnace.

The microstructure of the CVD coating was observed using a scanning electron microscope (SEM, Jeol JSM-6010PLUS/LA, Peabody, MA, USA) running at an accelerating voltage of 20 kV. In order to examine the distribution of different elements, both secondary electron images (SEI) and backscattering electron composition (BEC) images were captured. When the backscattering electron (BEC) images were taken, the acceleration voltage of 20 kV was used as well. The SEI images were compared with the BEC ones to obtain the composition distribution. Quantitative analysis of the composition of the material was conducted using energy dispersive X-ray spectroscopy (EDS).

To examine the conductive behavior of the coating, a CHI 440C electrochemical workstation (CH Instruments, Inc., Austin, TX, USA) was used operating in the potential scan mode to record the response of generated current (I) vs. the stimulating voltage (V). The Seebeck coefficient of the coating was measured by setting the specimen on a heating platform (heated by a TalBoys heater, Livonia, MI, USA) as shown in Figure 2. In the figure, "W" represents the working electrode lead. "R" represents

the reference electrode lead and "C" represents the counter electrode lead. The cold end and the hot end temperatures of the specimen were measured using an infrared thermometer. The CHI 440C electrochemical workstation was also used to record the open circuit voltage. A temperature sensing test was carried out using the same facility as for the Seebeck coefficient measurement. Figure 2a shows the schematic for measuring the Seebeck coefficient, while Figure 2b is a photograph showing the facility set-up. The infrared thermometer is not shown in the picture due to the required 120 mm vertical distance separation from the specimen.

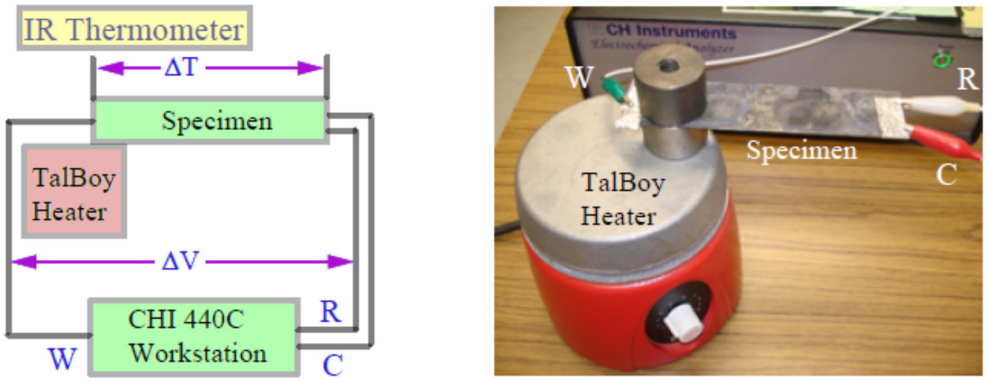

(**a**) (**b**)

Figure 2. Illustration and facility for Seebeck coefficient measurement and temperature sensing tests on the chemical vapor deposition (CVD) coating: (**a**) Sketch for measuring the Seebeck coefficient; (**b**) facility set-up.

3. Results and Discussion

The scanning electron microscopic (SEM) analysis results of the microstructure and the composition are presented in Figure 3. The SEM image for the coating in Figure 3a shows several morphological features including dendrites, pores, and clusters of materials. These features are evidence for a fast growing mechanism of the coating. This also indicates that the MOCVD of the Bi-Te-Ni-Fe coating followed a mass transport controlled mechanism. Figure 3b shows the area mapping results of the energy dispersive X-ray diffraction spectrum (EDS) of the coating. Obviously, the major elements in the coating include Bi, Te, Ni, and Fe as shown. The signals for Mg and O are mainly from the substrate, i.e., the MgO ceramic plate. Carbon signal is from the decomposing residues of the solvent DMF and the acetic functional group in nickel acetate and bismuth acetate. The quantitative results in both mass and atomic percentages are listed in Table 1. The EDS results in Table 1 show that the atomic ratio of O to Mg is slightly higher than 1. This is due to the tight bonding of C=O in the DMF. Some oxygen may go into the coating as impurity in the adsorption state at the grain boundaries of the coating material. Existing literature shows that Bi- and Te-oxide or nitrate can be fully reduced by 1 atm hydrogen at 400 or 500 °C [47,48]. NiO or nickel nitrate can also be reduced by hydrogen into metal at 500 °C [49]. Fe can be reduced at a low temperature of 300 °C [50]. Therefore the metal elements are unlikely to be in the oxidized state. Instead, the coating should be in the metallic state. From the data in the first two columns, it is estimated that the relative atomic ratio of Bi to Te is 3:1. This means that the coating is not a stoichiometric compound of Bi_2Te_3 as made be physical vapor deposition shown in open literature, e.g., in [51]. The reason for this is that tellurium (IV) chloride has lower vapor pressure than that of the organic compound, bismuth acetate. Due to the insufficient supply of Te, the Bi-rich phase was obtained under the high temperature reaction conditions. The advantage is that the resulting phase should be p-type due to the deficiency of Te, as will be confirmed by the Seebeck coefficient measurement. The Seebeck coefficient value for a p-type thermoelectric material should be positive.

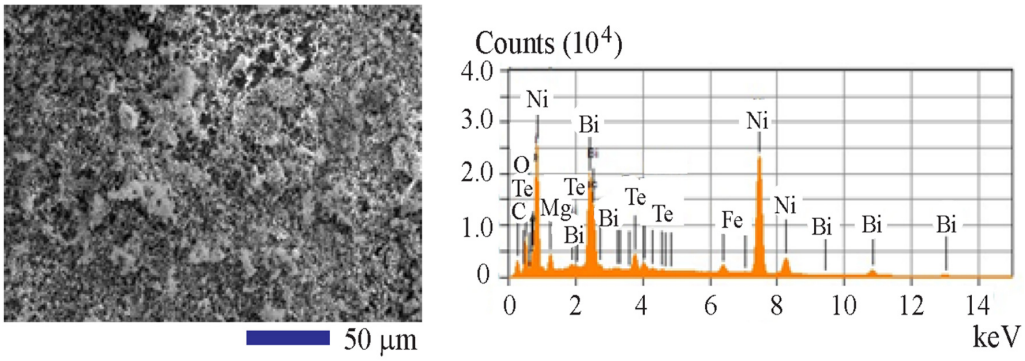

Figure 3. Scanning electron microscopic (SEM) image of the CVD coating and its composition profile: (**a**) secondary electron image (SEI) of the coating; (**b**) energy dispersive X-ray diffraction spectrum (EDS) showing the qualitative results of elements.

Table 1. Quantitative results of elemental composition from area mapping analysis.

Composition	Element						
	Bi	**Te**	**Ni**	**Fe**	**C**	**O**	**Mg**
wt %	24.87	5.15	50.13	1.95	6.57	5.63	5.70
at %	5.46	1.85	39.15	1.60	25.06	16.12	10.75

Figure 4a, a backscattering electron composition micrograph, reveals the distribution of the two heavy elements in the coating such as Te and Bi with very bright color while other light elements are shown in black color. To further reveal the distribution of the major elements, separate composition maps were captured. Figure 4b represents the distribution of Bi in green color. It can be seen that the Bi distribution matched the results as shown in the BEC image of Figure 4a. In Figure 4c, the distribution of Te represented by black color is shown. Evidently, the distribution of Te follows the pattern as for that of Bi. In Figure 4d, the Ni distribution in blue color is illustrated. From this map, it is found that Ni is uniformly distributed. We also generated the composition map for iron, a uniform distribution result (not shown here for simplicity) was found as well.

To obtain the composition information of some typical morphological features including dendrites, lumped clusters, and aggregates as illustrated in both Figures 3a and 4a, we did spot analysis on these features. In Figure 5a, three representative locations for the spot analysis are shown as Spot 001, Spot 002, and Spot 003. The qualitative results obtained from the three sites are given in Figure 5b–d, respectively. The composition details in relative mass percentage for each element from the three spots are presented in Table 2. The spectra in these three sub-figures illustrate the diffraction peaks from three major elements. One is Bi, another is Te, still another is Ni. At Spot 001, the highest peak of Bi is observed because it is the major element. The Ni peak is the second highest one. The Te signal follows them, resulting in the third highest peak. At Spot 002, Ni element shows the highest peak, indicating that the dark shaded region is a Ni-rich phase. At Spot 003, Mg appears as one of the major elements. This indicates that the aggregates with strong electron discharge represent microstructures from the ceramic substrate. The carbon signal comes from both Spots 002 and 003, revealing the carbon residues from the decomposition of the DMF solvent, nickel acetate, and bismuth acetate. While the oxygen signal mainly comes from the ceramic plate, MgO, it is also a residual element from the decomposition of the two metallic acetate salts and DMF. It is believed that the qualitative and quantitative elemental results from EDS spot analysis at 003 location also provide information that the oxidation state of the coating should be prevented because at this location, the atomic ratio of O to Mg is about 1.

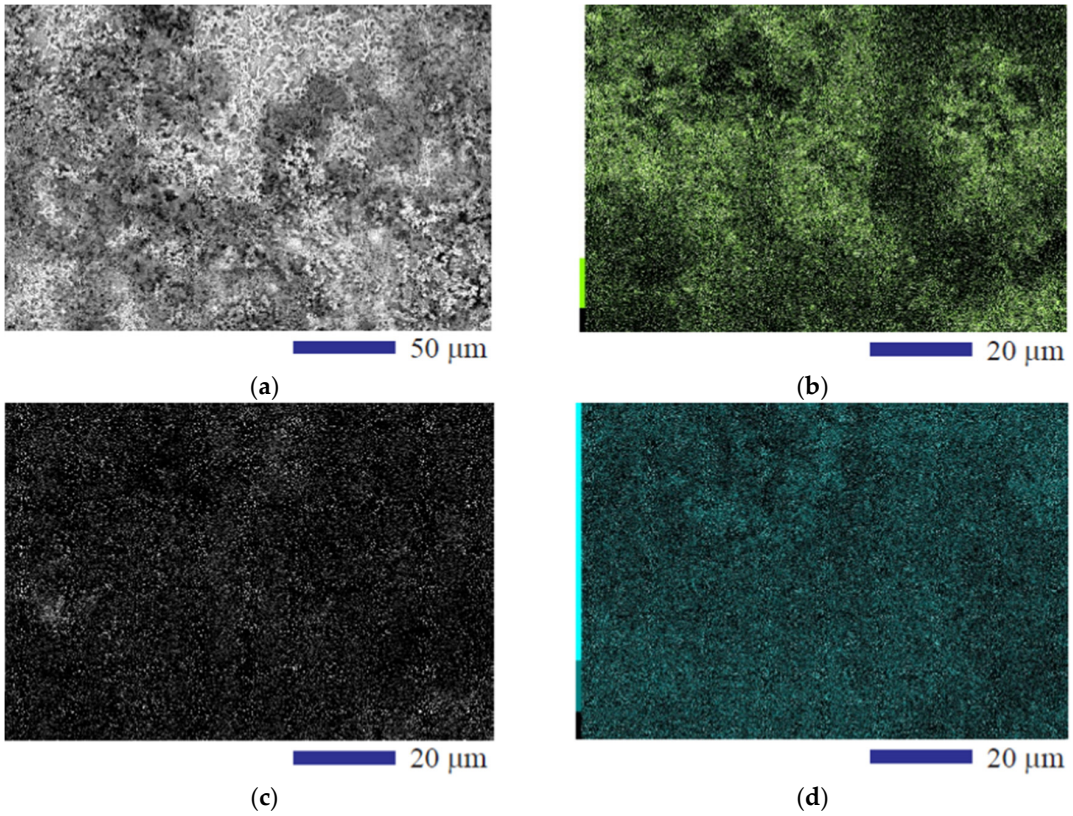

Figure 4. Backscattering electron composition (BEC) image of the CVD coating and its composition profile: (**a**) backscattering electron composition (BEC) image; (**b**) Bi composition map; (**c**) Te composition map; and (**d**) Ni composition map.

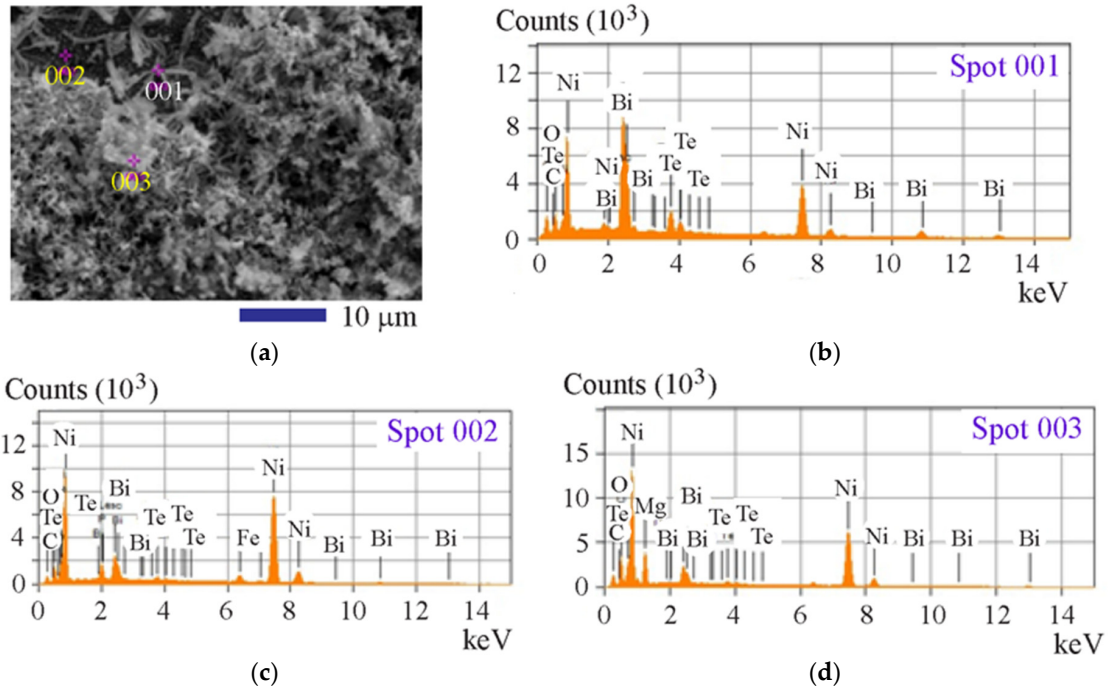

Figure 5. SEM spot analysis results: (**a**) SEM image showing the locations for the EDS spot analysis; (**b**) EDS spectrum for Spot 001; (**c**) EDS of Spot 002; (**d**) EDS of Spot 003.

Table 2. Quantitative results of elemental composition from spot analysis.

Element	wt %			
	Spot 1	Spot 2	Spot 3	Average
Bi	44.07	12.33	9.33	21.91
Te	10.97	1.87	2.03	4.96
Ni	30.59	68.21	48.06	48.06
Fe	3.85	2.95	0	2.45
Mg	0	0	19.08	6.04
O	10.53	5.33	10.29	8.27
C	0	6.77	6.60	4.26

It should be noted that X-ray diffraction (XRD) is a powerful tool to show the structure of the coating. Comparative studies on this new coating and traditional Bi_2Te_3 alloy using the XRD technique may be useful to reveal more information. Whether the coating is crystalline or not can also be determined through XRD. We predict that the structure of the two materials should be very similar. However, we did not take the structural studies as our main focus. This paper only shows the applicability of CVD processing in Bi-Te based complex alloys. More in-depth structure assessment work is an important topic for our future studies.

In order to characterize the electrically conductive behavior of the coating material, the CHI 440C electrochemical analyzer was used to generate the current, I, versus voltage, V, data. During the experiment, one end of the coating on the substrate was taken as the working electrode, which was wrapped by a strip of aluminum foil and held with a crocodile clip. The reference electrode lead and the counter electrode lead were connected together. The initial scan potential was 0.0 V. The final potential was 1.0 V, the scan rate was 0.01 V/s, and the temperature was 23 °C. Both scanning potential and corresponding current data were recorded and stored in a laptop computer. The variation of the current response vs. scan potential when the specimen was kept in the dark to level out the contribution of any photon induced current shows a similar trend from the I–V response measurements with the coating exposed to visible light. The results from the tests under ultraviolet (UV) light illumination also similar to those obtained under either visible light illumination or without any light illumination. This indicates that the specimen is not sensitive to visible light or UV light. The resistance estimated using the I–V data is about 28.57 Ω. The resistivity of the coating can be calculated using the formula as shown in [52];

$$\varrho = RbW/L \quad (1)$$

where R is the resistance of the coating, ϱ is the resistivity, and b is the thickness of the coating. The width of the coating is W and the length of the specimen is L. As mentioned earlier in Section 2, the thickness of the coating, b, is around 200 μm. The width of the specimen, W, is the same as the substrate of 38 mm, and the length of the specimen, L, is about 153 mm, the same as the MgO substrate. The resistivity of the coating (ϱ) calculated using Equation (1) is 1.419×10^{-3} (Ω·m). Then the conductivity of the coating is $\sigma = 1/\varrho = 704.61$ (S/m).

As compared with the published data for bulk Bi_2Te_3 [53], the conductivity of the coating from this work is only about one half of that of the existing Bi-Te bulk material. The main reasons for this include the size effect, microstructure effect, and the oxidation state effect. In this work, the thickness of the coating is smaller than that of the bulk material. Structurally, it is in porous or quasi-porous state. In addition, the decomposition of the two acetates and DMF introduces oxygen into the coating even with the hydrogen gas reduction. All these three effects could result in decreasing the conductivity of the coating material. The I–V response results not only provide information on the electrical conductive behavior of the coating, but also reveal that the excitation by photon energy does not change the conductivity of the coating, which validates that the coating has a narrow band structure.

Seebeck coefficients of thermoelectric materials can be determined using the derivative of potential vs temperature. In this work, we measured the potential vs temperature difference data. The average values from seven tests for each temperature difference condition are shown in Table 3. Based on the data in Table 3, a voltage (V) vs temperature (T) plot was established and shown in Figure 6. The contribution to the thermoelectric voltage by the aluminum foil and silver-gold alloy plated electrodes, which is at micro volt level, was subtracted from the raw data. Error bars are shown in Figure 6 to reveal the scattering of the data obtained from seven tests for each point. The temperature difference refers to the difference between the hot end and the cold end in the test set-up as illustrated in Figure 2. The Seebeck coefficient of the coating was obtained from the slope of the V–T curve as 179 μV/K. Since the Seebeck coefficient is positive, it means that the coating material prepared in this work is p-type. The value is slightly higher than that reported in [53]. In [53], the value of the Seebeck coefficient for the p-type bulk Bi_2Te_3 alloy is 165 μV/K. The possible reason for the higher Seebeck coefficient value of the coating than that of the bulk material is that the electron mobility in the coating should be lower than that in the bulk material. A higher electrical potential can develop in the coating due to the confinement of the electrons in the dendritic and porous structures. Therefore, the Seebeck coefficient is increased for the coating as prepared in this work. Microstructure especially the porous structure becomes a reason for reducing the mobility of electrons. Therefore, a higher value of Seebeck coefficient could be obtained. Although we have not conducted extensive studies on this issue, it is meaningful to tune the microstructure of the films and correlate it with the Seebeck coefficient of the material as one of the future tasks.

Table 3. Voltage measured at different hot end temperatures for Seebeck coefficient calculation. The cold end temperature was kept as 23 °C.

Temperature Difference (°C)	Voltage (mV)
2	0.2797
6	1.1350
10	1.4843
15	2.8284
18	3.0625

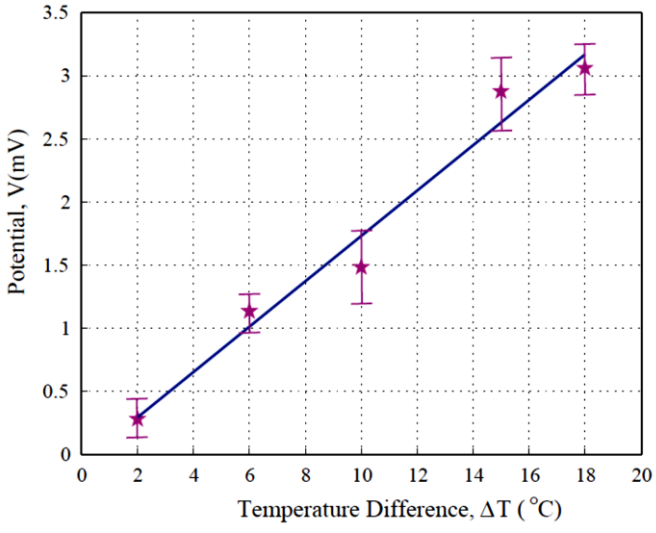

Figure 6. Plot for determining the Seebeck coefficient of the coating.

It is worth exploring the potential applications of this coating. The possible applications of the coating include thermoelectric energy conversion and temperature sensing. As is known, planar temperature sensors are useful in measuring temperatures of viscous fluids, for example, in polymer processing [54]. The variation of thermoelectric potential versus temperature change was tested using

the facility as shown in Figure 2b. Two cylindrical steel blocks were used as heat sinks setting on the top of the heater. As the controller gave the signal for heating, the temperature of the hot end of the specimen sandwiched between the two heat sinks increased. The cold end was set at the room temperature of 23 °C. Once the hot end temperature reached a set point, the electricity was cut off and the heat sinks were cooled down. The output data of the electric potential due to the Seebeck effect of the coating at different time frames were recorded by the CHI440C. Then, the data were plotted and shown in Figure 7. The temperature data sets are also shown in Figure 7 as open circles.

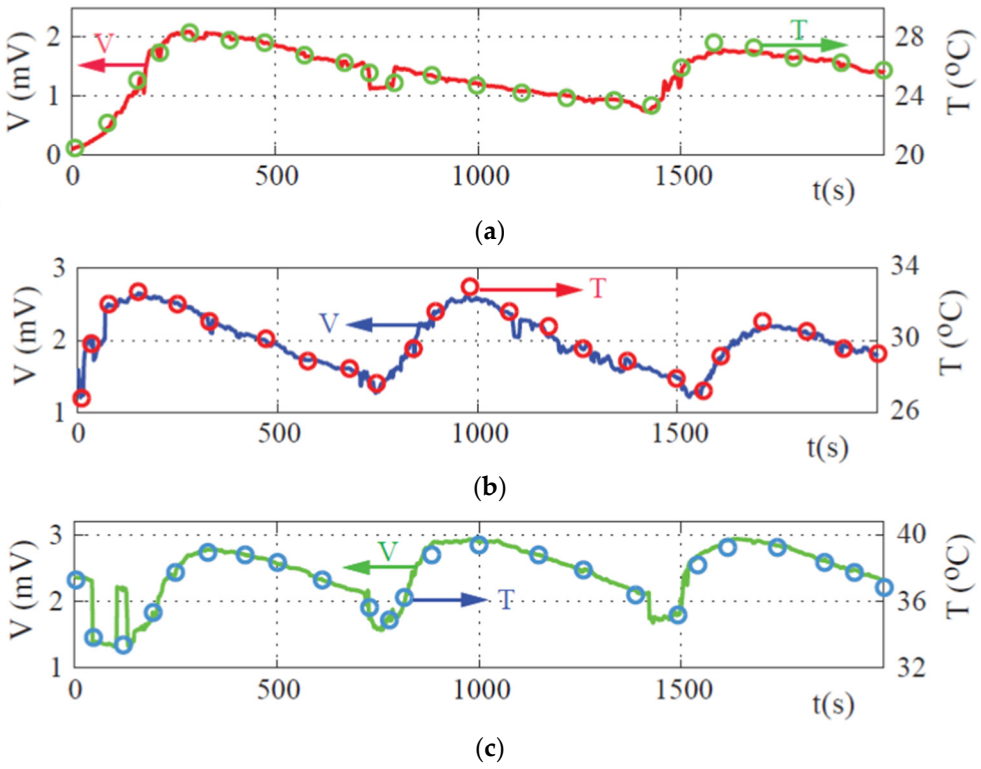

Figure 7. Time dependent thermoelectric responses to show the temperature sensing performance of the coating with the 5 °C temperature variation at the hot end with a constant cold end temperature of 23 °C: (**a**) hot end temperature changes between 23 and 28 °C; (**b**) hot end temperature changes between 28 and 33 °C; (**c**) hot end temperature changes between 33 and 38 °C.

Figure 7a shows the temperature sensing behavior when the temperature of the heat sinks varied between 23 and 28 °C. The results in Figure 7a can also be viewed as the time dependent open circuit potential profile when the hot end underwent a temperature difference of 5 °C. Similar measurement was conducted when the temperatures changed in the ranges from 28 to 33 °C and from 33 to 38 °C. In Figure 7b the voltage vs time profile was illustrated based on the hot end temperature variation from 28 to 33 °C. The voltage vs time profile for the case of temperature variation from 33 to 38 °C is demonstrated in Figure 7c. The data presented in Figure 7 provide information on the temperature sensing behavior of the coating. The time dependent behavior shows how fast the response is. In addition, the repeatability and the stability of thermoelectric potential vs time t are represented by this figure. From the three subplots, we can see that the coating can capture the tiny changes of the temperature in the two heat sinks. This shows a relative high sensitivity of the thermoelectric potential of the coating to the temperature variations.

It must be noted that the data presented here just show the thermoelectric responses of the coating. Thermal conductive behavior should be investigated as well. The challenge is that the coating on MgO formed a composite system. How to measure the phonon transfer in the thin film remains an interesting topic for future studies. To measure the thermal conductivity of the thin coating,

transient methods such as laser flash testing coupled with atomic force microscopic analysis may work. Computational materials engineering has been found useful for prediction of the Seebeck coefficient. As shown in [55], the predicted highest absolute value of Seebeck coefficient for the Bi-Te alloy is 300 μV/K. By optimizing the carrier concentration in an n-typed Pb-Te alloy, the Seebeck effect can be enhanced [56]. Both the computation analysis and the carrier concentration optimization will be directions for further improving the thermoelectric property of the coating. Comparing with the prior work especially the nanomaterials as shown in Table 4, it can be seen that most of the cited studies showed lower *S* values than the current work with the exception of ref. [57]. It can be concluded that thin film, nanostructured materials are promising in the enhancement of thermoelectricity. Ref. [57] is comparable to this work because Bi nanoparticles were introduced into the Bi_2Te_3 matrix so that the Bi/Bi_2Te_3 interface formed in the nanocomposite. This interface showed a potential barrier and resulted in the effect of low-energy electron filtering. Consequently, an enhanced Seebeck coefficient was obtained. The advantage of this work over that introduced by ref. [57] lies in the one step MOCVD, which is much simpler with respect to processing. In [57], multiple steps were used for making the two components for nanocomposite processing, i.e., mechanical milling for Bi_2Te_3 preparation and chemical processing of Bi nanoparticles.

Table 4. Comparison on the absolute value of Seebeck coefficient, *S*, for different materials.

Materials	*S* (μV/K)	Source
Bi-Te-Ni-Fe	179	This work
Bulk Bi-Se	80	[58]
Bi-Se Coating	122	[58]
Bi-Te Carbon Nanotube	34	[59]
Bi-Te Polyaniline	31	[60]
Bi/Bi-Te Nanocomposite	185	[57]
Graphene	90	[61]

4. Conclusions

Complex Bi-Te-Ni-Fe coating material has been made by a one-pot precursor approach. The material in coating form can be deposited on a magnesium oxide ceramic substrate by the ambient pressure chemical vapor deposition (CVD) technique. Nickel acetate, bismuth acetate, iron (III) nitrate, and tellurium (IV) chloride were dissolved in *N*,*N*-dimethylformamide (DMF) to form precursors of the metal sources for Ni, Bi, Fe, and Te. Hydrogen can be used as carrier gas to prevent deep oxidation of the thermoelectric coating material. At 500 °C, the deposition rate reached about 100 μm/h. The MOCVD is a mass transport limiting process. The microstructure of the deposited coating as revealed by scanning electron microscopic analysis contains needle-like submicron dendrites and aggregated fine particles. The needle-like dendrites form networks with fairly uniform distribution on the substrate. Thermoelectric property tests show that the MOCVD coating is p-type with a Seebeck coefficient of 179 μV/K. This value is higher than those of most existing bulk Bi-Te alloys and comparable to that of the Bi/Bi_2Te_3 nanocomposite, revealing that the coating material has better thermoelectric energy conversion performance than its bulk counterpart. Time-dependent potential measurements showed accurate changes in the temperature profiles at the surfaces of the heat sinks. It can be concluded that thin film, nanostructured materials are promising for the enhancement of the Seebeck coefficient.

Acknowledgments: This work was supported by the US National Science Foundation (NSF) under Grant Number CMMI-1333044. The SEM images were made possible by the support from the National Science Foundation under Grant Number DMR-1429674. Yong X. Gan acknowledges the 2016–2017 and 2017–2018 Provost's Teacher Scholar support. The California State Polytechnic University Pomona internal supports through a 2016–2017 RSCA grant and a 2016–2017 SPICE grant are also gratefully acknowledged. We appreciate the three reviewers for providing constructive comments on modifying the paper.

Author Contributions: Yong X. Gan and Mingheng Li conceived and designed the experiments; Jeremy B. Gan and Yong X. Gan performed the CVD experiments; Anan S. Hamdan and Yong X. Gan examined the microstructure of the coating; J.B.G. contributed to the data analysis; Yong X. Gan wrote the paper.

Conflicts of Interest: The authors declare no conflict of interest.

References

1. Huang, G.; Jian, J.; Lei, R.; Cao, B. Single-crystalline Bi_2Se_3 nanowires grown by catalyst-free ambient pressure chemical vapor deposition. *Mater. Lett.* **2016**, *179*, 198–201. [CrossRef]
2. Tynell, T.; Aizawa, T.; Ohkubo, I.; Nakamura, K.; Mori, T. Deposition of thermoelectric strontium hexaboride thin films by a low pressure CVD method. *J. Cryst. Growth* **2016**, *449*, 10–14. [CrossRef]
3. Chen, P.; Wang, J.; Lu, Y.; Zhang, S.; Liu, X.; Hou, W.; Wang, Z.; Wang, L. The fabrication of ReS_2 flowers at controlled locations by chemical vapor deposition. *Phys. E Low-Dimens. Syst. Nanostruct.* **2017**, *89*, 115–118. [CrossRef]
4. Haase, A.; Peters, A.; Rosiwal, S. Growth and thermoelectric properties of nitrogen-doped diamond/graphite. *Diam. Relat. Mater.* **2016**, *63*, 222–226. [CrossRef]
5. Hewitt, C.A.; Carroll, D.L. The effects of acid treatment on the thermoelectric power of multiwalled carbon nanotubes synthesized by chemical vapor deposition. *Chem. Phys. Lett.* **2013**, *580*, 67–72. [CrossRef]
6. Kunadian, I.; Lipka, S.M.; Swartz, C.R.; Qian, D.; Andrews, R. Determination of carrier densities of boron- and nitrogen-doped multiwalled carbon nanotubes using Mott-Schottky plots. *J. Electrochem. Soc.* **2009**, *156*, K110–K115. [CrossRef]
7. Cademartiri, L.; Ozin, G.A. Ultrathin nanowires—A materials chemistry perspective. *Adv. Mater.* **2009**, *21*, 1013–1020. [CrossRef]
8. Balducci, A.; Marinelli, M.; Morgada, M.E.; Pucella, G.; Rodriguez, G.; Scoccia, M.; Verona-Rinati, G. CVD-diamond-based thermocouple for high sensitive temperature measurements. *Microsyst. Technol.* **2006**, *12*, 365–368. [CrossRef]
9. Balducci, A.; D'Amico, A.; Di Natale, C.; Marinelli, M.; Milani, E.; Morgada, M.E.; Pucella, G.; Rodriguez, G.; Tucciarone, A.; Verona-Rinati, G. High performance CVD-diamond-based thermocouple for gas sensing. *Sens. Actuators B* **2005**, *111*, 102–105. [CrossRef]
10. Eaton, S.C.; Anderson, A.B.; Angus, J.C.; Evstefeeva, Y.E.; Pleskov, Y.V. Diamond growth in the presence of boron and sulfur. *Diam. Relat. Mater.* **2003**, *12*, 1627–1632. [CrossRef]
11. Horiuchi, R.; Okano, K.; Rupesinghe, N.; Chhowalla, M.; Amaratunga, G.A.J. Seebeck measurements of N-doped diamond thin film. *Phys. Stat. Sol. A* **2002**, *193*, 457–461. [CrossRef]
12. Souw, E.K.; Meilunas, R.J.; Szeles, C.; Ravindra, N.M.; Tong, F.M. Photoconductivity of CVD diamond under bandgap and subbandgap irradiations. *Diam. Relat. Mater.* **1997**, *6*, 1157–1171. [CrossRef]
13. Saitoh, H.; Ishikawa, M.; Urao, R. Substrate temperature measured by a film-on-plate thermocouple during diamond growth using the combustion flame technique. *Diam. Relat. Mater.* **1995**, *4*, 1056–1060. [CrossRef]
14. DaVila, D.; Tarancon, A.; Calaza, C.; Salleras, M.; Fernandez-Regulez, M.; San Paulo, A.; Fonseca, L. Improved thermal behavior of multiple linked array of silicon nanowires integrated into planar thermoelectric microgenerators. *J. Electron. Mater.* **2013**, *42*, 1918–1925. [CrossRef]
15. Wu, Y.; Fan, R.; Yang, P. Block-by-block growth of single-crystalline Si/SiGe superlattice nanowires. *Nano Lett.* **2002**, *2*, 83–86. [CrossRef]
16. Kim, J.G.; Choi, Y.Y.; Choi, D.J.; Choi, S.M. Study on the thermoelectric properties of CVD SiC deposited with inert gases. *J. Electron. Mater.* **2011**, *40*, 840–844. [CrossRef]
17. Kim, J.G.; Choi, Y.Y.; Choi, D.J.; Kim, J.I.; Kim, B.S.; Choi, S.M. A study on the thermoelectric property of chemical vapor deposited SiC films with temperature and diluent gases variations. *J. Ceram. Soc. Jan.* **2009**, *117*, 574–577. [CrossRef]
18. Tajima, K.; Shin, W.; Murayama, N.; Itoh, T.; Izu, N.; Matsubara, I. Preparation of phosphorus-doped $Si_{0.8}Ge_{0.2}$ thermoelectric thin films using RF sputtering with induction coil. *J. Ceram. Soc. Jan.* **2005**, *113*, 558–561. [CrossRef]
19. Yoshinaga, M.; Iida, T.; Noda, M.; Endo, T.; Takanashi, Y. Bulk crystal growth of Mg_2Si by the vertical Bridgman method. *Thin Solid Films* **2004**, *461*, 86–89. [CrossRef]

20. Mukaida, M.; Hiyama, I.; Tsunoda, T.; Imai, Y. Preparation of β-$FeSi_2$ films by chemical vapor deposition. *Thin Solid Films* **2001**, *381*, 214–218. [CrossRef]
21. Akiyama, K.; Ohya, S.; Funakubo, H. Preparation of β-$FeSi_2$ thin film by metal organic chemical vapor deposition using iron-carbonyl and mono-silane. *Thin Solid Films* **2004**, *461*, 40–43. [CrossRef]
22. Kumashiro, Y.; Nakamura, K.; Enomoto, T.; Tanaka, M. Preparation and thermoelectric properties of BP films on SOI and sapphire substrates. *J. Mater. Sci. Mater. Electron.* **2011**, *22*, 966–973. [CrossRef]
23. Komatsu, S.; Sato, Y.; Hirano, D.; Nakamura, T.; Koga, K.; Yamamoto, A.; Nagata, T.; Chikyo, T.; Watanabe, T.; Takizawa, T.; et al. P-type sp^3-bonded BN/n-type Si heterodiode solar cell fabricated by laser-plasma synchronous CVD method. *J. Phys. D Appl. Phys.* **2009**, *42*, 225107. [CrossRef]
24. Wang, Z.; Shimizu, Y.; Sasaki, T.; Kirihara, K.; Kawaguchi, K.; Kimura, K.; Koshizaki, N. Fabrication of crystallized boron films by laser ablation. *J. Solid State Chem.* **2004**, *177*, 1639–1645. [CrossRef]
25. Kumashiro, Y.; Enomoto, T.; Sato, K.; Abe, Y.; Hirata, K.; Yokoyama, T. Thermoelectric properties of photo- and thermal CVD boron and boron phosphide films. *J. Solid State Chem.* **2004**, *177*, 529–532. [CrossRef]
26. Kumashiro, K.; Hirata, K.; Sato, K.; Yokoyama, T.; Aisu, T.; Ikeda, T.; Minaguchi, M. Thermoelectric properties of boron and boron phosphide films. *J. Solid State Chem.* **2000**, *154*, 26–32. [CrossRef]
27. Kumashiro, Y.; Yokoyama, T.; Sato, A.; Ando, Y. Thermoelectric properties of boron and boron phosphide CVD wafers. *J. Solid State Chem.* **1997**, *133*, 314–321. [CrossRef]
28. Suematsu, H.; Kitajima, K.; Ruiz, I.; Kobayashi, K.; Takeda, M.; Shimbo, D.; Suzuki, T.; Jiang, W.; Yatsui, K. Thermoelectric properties of crystallized boron carbide thin films prepared by ion-beam evaporation. *Thin Solid Films* **2002**, *407*, 132–135. [CrossRef]
29. Sezer, A.O.; Brand, J.I. Chemical vapor deposition of boron carbide. *Mater. Sci. Eng. B* **2001**, *79*, 191–202. [CrossRef]
30. Kumasiro, Y.; Yokoyama, T.; Sakamoto, T.; Fujita, T. Preparation and electrical properties of boron and boron phosphide films obtained by gas source molecular beam deposition. *J. Solid State Chem.* **1997**, *133*, 269–272. [CrossRef]
31. Ngamou, P.H.T.; Bahlawane, N. Chemical vapor deposition and electric characterization of perovskite oxides $LaMO_3$ (*M* = Co, Fe, Cr and Mn) thin films. *J. Solid State Chem.* **2009**, *182*, 849–854. [CrossRef]
32. Cho, H.S.; Kamins, T.I. In situ control of Au catalyzed chemical vapor deposited (CVD) Ge nanocone morphology by growth temperature variation. *J. Cryst. Growth* **2010**, *312*, 2494–2497. [CrossRef]
33. Grigorian, L.; Fang, S.; Sumanasekera, G.; Rao, A.M.; Schrader, L.; Eklund, P.C. Physical properties of CVD-grown Se-carbon films. *Synth. Met.* **1997**, *87*, 211–217. [CrossRef]
34. Giani, A.; Boulouz, A.; Pascal-Delannoy, F.; Foucaran, A.; Boyer, A. MOCVD growth of Bi_2Te_3 layers using diethyltellurium as a precursor. *Thin Solid Films* **1998**, *315*, 99–103. [CrossRef]
35. Giani, A.; Boulouz, A.; Pascal-Delannoy, F.; Foucaran, A.; Boyer, A. Growth of Bi_2Te_3 and Sb_2Te_3 thin films by MOCVD. *Mater. Sci. Eng. B* **1999**, *64*, 19–24. [CrossRef]
36. Venkatasubramanian, R.; Colpitts, T.; Watko, E.; Lamvik, M.; E1-Masry, N. MOCVD of Bi_2Te_3, Sb_2Te_3 and their superlattice structures for thin-film thermoelectric applications. *J. Cryst. Growth* **1997**, *170*, 817–821. [CrossRef]
37. Bendt, G.; Schulz, S.; Zastrow, S.; Nielsch, K. Single-source precursor-based deposition of Sb_2Te_3 films by MOCVD. *Chem. Vap. Depos.* **2013**, *19*, 235–241.
38. Kang, S.W.; Jeon, K.M.; Shin, J.S.; Chun, J.R.; Kim, Y.H.; Lee, S.J.; Yun, J.Y. MOCVD of c-oriented Bi_2Te_3 films on SiO_2 substrates using triethyl bismuth and di-tertiarybutyl tellurium. *Chem. Vap. Depos.* **2013**, *19*, 61–67. [CrossRef]
39. Alegria, L.D.; Yao, N.; Petta, J.R. MOCVD synthesis of compositionally tuned topological insulator nanowires. *Phys. Stat. Solidi-Rapid Res. Lett.* **2014**, *8*, 991–996. [CrossRef]
40. Benjamin, S.L.; de Groot, C.H.; Gurnani, C.; Hector, A.L.; Huang, R.; Koukharenko, E.; Levasona, W.; Reid, G. Controlling the nanostructure of bismuth telluride by selective chemical vapour deposition from a single source precursor. *J. Mater. Chem. A* **2014**, *2*, 4865–4869. [CrossRef]
41. Hatanpaa, T.; Ritala, M.; Leskela, M. Precursors as enablers of ALD technology: Contributions from University of Helsinki. *Coord. Chem. Rev.* **2013**, *257*, 3297–3322. [CrossRef]
42. Cao, H.L.; Venkatasubramanian, R.; Liu, C.; Pierce, J.; Yang, H.R.; Hasan, M.Z.; Wu, Y.; Chen, Y.P. Topological insulator Bi_2Te_3 films synthesized by metal organic chemical vapor deposition. *Appl. Phys. Lett.* **2012**, *101*, 162104. [CrossRef]

43. You, H.; Baek, S.H.; Kim, K.C.; Kwon, O.J.; Kim, J.S.; Park, C. Growth and thermoelectric properties of Bi_2Te_3 films deposited by modified MOCVD. *J. Cryst. Growth* **2012**, *346*, 17–21. [CrossRef]
44. Sun, Z.L.; Liufu, S.C.; Liu, R.H.; Chen, X.H.; Chen, L.D. A general strategy to bismuth chalcogenide films by chemical vapor transport. *J. Mater. Chem.* **2011**, *21*, 2351–2355. [CrossRef]
45. Kwon, S.D.; Ju, B.K.; Yoon, S.J.; Kim, J.S. Fabrication of bismuth telluride-based alloy thin film thermoelectric devices grown by metal organic chemical vapor deposition. *J. Electron. Mater.* **2009**, *38*, 920–924. [CrossRef]
46. Kwon, S.D.; Kim, J.S. MOCVD growth of thermoelectric $BiSbTe_3$ films on surface-treated sapphire substrates. *J. Korean Phys. Soc.* **2009**, *54*, 1589–1593. [CrossRef]
47. Bochentyn, B.; Karczewski, J.; Miruszewski, T.; Kusz, B. Structure and thermoelectric properties of Bi-Te alloys obtained by novel method of oxide substrates reduction. *J. Alloy. Compd.* **2015**, *646*, 1124–1132. [CrossRef]
48. Gan, Y.X.; Chen, A.D.; Gan, R.Y.; Hamdan, A.S. Energy conversion behaviors of antimony telluride particle loaded partially carbonized nanofiber composite mat manufactured by electrohydrodynamic casting. *Microelectron. Eng.* **2017**, *181*, 16–21. [CrossRef]
49. Xiang, J.; Shen, X.; Song, F.; Liu, M.; Zhou, G.; Chu, Y. Fabrication and characterization of Fe–Ni alloy/nickel ferrite composite nanofibers by electrospinning and partial reduction. *Mater. Res. Bul.* **2011**, *46*, 258–261. [CrossRef]
50. Ji, Y.; Zhang, X.; Zhu, Y.; Li, B.; Wang, Y.; Zhang, J.; Feng, Y. Nickel nanofibers synthesized by the electrospinning method. *Mater. Res. Bull.* **2013**, *48*, 2426–2429. [CrossRef]
51. Zhang, G.; Yu, Q.; Wang, W.; Li, X. Nanostructures for thermoelectric applications: Synthesis, growth mechanism, and property studies. *Adv. Mater.* **2010**, *22*, 1959–1962. [CrossRef] [PubMed]
52. Callister, W.D., Jr.; Rethwisch, D.G. *Materials Science and Engineering: An Introduction*, 9th ed.; John Wiley and Sons, Inc.: Hoboken, NJ, USA, 2014; pp. 726–729.
53. Goldsmid, H.J. Bismuth telluride and its alloys as materials for thermoelectric generation. *Materials* **2014**, *7*, 2577–2592. [CrossRef] [PubMed]
54. Debey, D.; Bluhm, R.; Habets, N.; Kurz, H. Fabrication of planar thermocouples for real-time measurements of temperature profiles in polymer melts. *Sens. Actuators A* **1997**, *58*, 179–184. [CrossRef]
55. Wimmer, E.; Christensen, M.; Eyert, V.; Wolf, W.; Reith, D.; Rozanska, X.; Freeman, C.; Saxe, P. Computational materials engineering: Recent applications of VASP in the MedeA® software environment. *J. Korean Ceram. Soc.* **2016**, *53*, 263–272. [CrossRef]
56. Pei, Y.; Gibbs, Z.M.; Gloskovskii, A.; Balke, B.; Zeier, W.G.; Snyder, G.J. Optimum carrier concentration in n-type PbTe thermoelectrics. *Adv. Energy Mater.* **2014**, *4*, 1400486. [CrossRef]
57. Sumithra, S.; Takas, N.J.; Misra, D.K.; Nolting, W.M.; Poudeu, P.F.P.; Stokes, K.L. Enhancement in thermoelectric figure of merit in nanostructured Bi_2Te_3 with semimetal nanoinclusions. *Adv. Energy Mater.* **2011**, *1*, 1141–1147. [CrossRef]
58. Sun, Y.; Cheng, H.; Gao, S.; Liu, Q.; Sun, Z.; Xiao, C.; Wu, C.; Wei, S.; Xie, Y. Atomically thick bismuth selenide freestanding single layers achieving enhanced thermoelectric energy harvesting. *J. Am. Chem. Soc.* **2012**, *134*, 20294–20297. [CrossRef] [PubMed]
59. Pang, H.; Piao, Y.Y.; Tan, Y.Q.; Jiang, G.Y.; Wang, J.H.; Li, Z.M. Thermoelectric behavior of segregated conductive polymer composites with hybrid fillers of carbon nanotube and bismuth telluride. *Mater. Lett.* **2013**, *107*, 150–153. [CrossRef]
60. Chatterjee, K.; Suresh, A.; Ganguly, S.; Kargupta, K.; Banerjee, D. Synthesis and characterization of an electro-deposited polyaniline-bismuth telluride nanocomposite—A novel thermoelectric material. *Mater. Charact.* **2009**, *60*, 1597–1601. [CrossRef]
61. Mahmoud, L.; Alhwarai, M.; Samad, Y.A.; Mohammad, B.; Laio, K.; Elnaggar, I. Characterization of a graphene-based thermoelectric generator using a cost-effective fabrication process. *Energy Procedia* **2015**, *75*, 615–620. [CrossRef]